

Bachelor Thesis

Finding an Optimal Regularisation Parameter for the Inversion of Transient Electromagnetic Data Using the L-Curve Method

Peter Balogh

e12202337@student.tuwien.ac.at

Matr.Nr. 1220 2337

Date: July 27, 2025

Supervisor: Associate Prof. Dr.rer.nat. Adrian Flores-Orozco

Abstract

1 Introduction

2 Materials and Methods

2.1 State of the Art

2.2 Experimental Set up

In order to investigate the applicability of automatically determining an optimal lambda value to TEM data, we conducted a field survey in October of 2024 at the Martenhofer Lacke in the Nationalpark Neusiedlersee - Seewinkel. The Geophysics Research Unit at TU Wien kindly provided data from May 2024 for the same location but with a differing measuring configuration, which enables a comparison between varying setups.

Furthermore a python package was developed to read, filter, and invert the TEM data. The visualisation of an L-curve as well as several methods of automatically finding an optimal lambda were also implemented.

2.2.1 Measuring Device

Both surveys were conducted with the TEM-Fast 48 HPC system by Applied Electromagnetic Research (AEMR). It is a compact device allowing the use of a single-loop configuration. By connecting an external 12 / 24 V battery a current either 1 / 4 A can be put through the connected transmitter loop. It records up to 48 logarithmically spaced time gates, which results in a time range between 4–16000 μ s. The specific number of time gates can be chosen through a time-key. Table 1 shows which time-key leads to which recording time range. To provide an optimal signal-to-noise ratio the device automatically stacks multiple pulses (Barsukov et al. 2015). The number of stacks are given by the formula $P_{tot} = 13 \times n_s \times n_{as}$ (Aigner et al. 2021), where n_s (1–20) is the chosen stacking-key and n_{as} is the number of analogue stacks depending on the chosen time-key and can be found in Table 1. More detailed information on the device can be found in the manual provided on the website <http://www.aemr.net/tem-fast.htm>.

Tab. 1: Parameters relating to the time-key of the TEM-FAST 48 HPC system (Excerpt from the manual).

Key	Max Time (μs)	Time Gates	Analogue Stacks
1	64	16	1024
2	128	20	512
3	256	24	256
4	512	28	128
5	1024	32	64
6	2048	36	32
7	4096	40	16
8	8192	44	8
9	16384	48	4

2.2.2 Field Survey

The field measurements were carried out at the Martenhofer Lacke in the *Nationalpark Neusiedlersee - Seewinkel* ($16^{\circ} 51' 23.058''$ N, $47^{\circ} 45' 8.4348''$ E), which is located on the east side of the Neusiedler See, Austria. Being part of the Seewinkel, which are intermittent alkaline soda waters, this water cycle of this lake is fueled by deep saline groundwater and evaporation leading to its high salinity and shallow water depth, which also varies throughout the year (Boros et al. 2025). This location was chosen due to having sparse man-made structures in the Nationalpark, which reduces noise in the gathered data to a minimum (Aigner et al. 2024).

The first survey, consisting of 45 soundings as shown in Figure 1 with a 12.5×12.5 m loop, was carried out on the 22nd May 2024 and for the second survey 66 soundings, visualised in Figure 2 with a 6.25×6.25 m loop were measured on 8th October 2024. For both surveys a Voltage of 24V was used and Table 2 shows the parameters for each sounding. Based upon a first visual inspection of the data some soundings were marked as "anomalous" as seen in Figures 1 and 2.

2.2.3 Python Package

In order to process the gathered data, we developed a python package mainly based on open-source python libraries. For the inversion routine we built upon the work of Aigner et al. (2021), which combines the electromagnetic wave modelling capabilities of `empymod` (Werth-

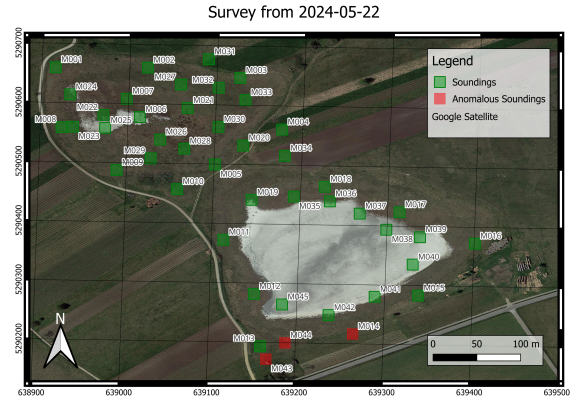


Fig. 1: Locations of all the TEM soundings measured in the first survey (22nd May 2024), where soundings are marked as anomalies, which fell out of order in a first visual inspection.

müller 2017) with the inversion algorithm from PyGIMLi (Rücker et al. 2017).

The capabilities of this package include the reading of TEM data, adding coordinates to each sounding, the filtering based upon a time intervall, and the visualisation of the raw with the filtered data. The inversion routine requires certain starting parameters like the lambda value, a layer distribution, a start model, and the relative error of the measured signal. If not specified otherwise a homogeneous model with the median apparent resistivity of the sounding is used as the starting model and the relative error is computed based of the error output of the measuring device. In case of particularly noisy data it is possible to set a minimum value for the relative error (noise floor). The noise floor

Tab. 2: Device settings used as well as the resulting measured time ranges and total number of pulses stacked for each sounding of both surveys.

Sounding	Current	Time Range	Time Key	Stacking Key	Total Stacks
22nd May 2024					
M001, M002	4.1 A	4 – 480 μ s	4	3	4992
M003 – M014	1.0 A	4 – 480 μ s	4	3	4992
M015 – M045	1.0 A	4 – 240 μ s	3	3	9984
8th October 2024					
M001 – M066	4.1 A	4 – 240 μ s	3	5	16640

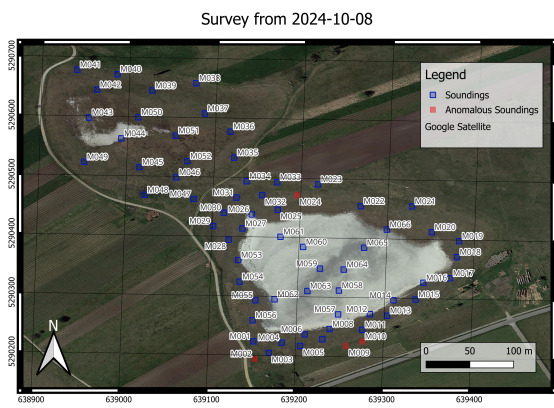


Fig. 2: Locations of all the TEM soundings measured in the second survey (8th October 2024), where soundings are marked as anomalies, which fell out of order in a first visual inspection.

limits how strongly the inversion algorithm tries to fit the model to each data point to avoid fitting errors. This inversion algorithm works with a model of the subsurface, where a resistivity value is assigned to a layer with a certain thickness, and only modifies the resistivity value of every layer while keeping the thicknesses fixed. This makes the choice of an appropriate layer distribution (specifying the number and thicknesses of layers) vital (Welkens 2025).

We also implemented the functionality to compute and visualise an L-Curve for a TEM sounding. For this we run the inversion for various logarithmically spaced lambda values, specified by the lower bound, the upper bound, and the number of values. For each inversion, we compute the root-mean-square (RMS) misfit of the data with the model as well as the roughness of the model and use these two values as the coordinates of a point corresponding

to each inversion, which should result in an L-Curve (Culturera et al. 2020; Hansen 1999).

To find an optimal lambda value for the inversion we implemented several search algorithms, which all try to find the point (corresponding to a lambda value) with the highest curvature on the L-Curve (Lloyd et al. 1997; Culturera et al. 2020). We implemented the method used by Lloyd et al. (1997), which fits a cubic spline function to the L-Curve and computes the first and second derivative of this function, which are used to compute the curvature of the function at each point. We also implemented a similar approach, where we used the `numpy.gradient` function (<https://numpy.org/doc/1.26/reference/generated/numpy.gradient.html>) to compute the first and second derivative for the curvature. Lastly we implemented the iterative golden section search algorithm as described by Culturera et al. (2020), where a lower and upper bound is defined for the lambda value and by comparing two curvatures within the interval and discarding the lower one, this method contracts the interval towards the optimal lambda. The advantage compared to the other two methods is that it is not bound to the predefined list of logarithmically spaced lambda values, which in theory allows a more precise determination of the optimal lambda.

3 Results

The data gathered in the two surveys was processed separately. Upon a visual inspection of apparent resistivity curves, which make minor differences more distinguishable than the signal curves, the soundings were split into two groups: The majority of soundings which follow a clear

trend, which we will reference as "normal soundings" and some soundings which do not align with the trend will be referenced as "anomalous soundings".

3.1 Filtering of the Data

Figure 3 shows the normal soundings of the first survey (22nd May 2024) with the 12.5×12.5 m loop and Figure 4 shows the anomalies. In Figure 3(b) it can be clearly seen that the effects of the turn-off ramp as described by Aigner et al. (2021) influence the measurements until about $8 \mu\text{s}$, which aligns with the $4.2 - 8.6 \mu\text{s}$, found by Aigner et al. (2021). At about $240 \mu\text{s}$ Figure 3(b) shows how the various curves start having distortions and Figure 3(a) shows that measured impulse response is becoming a similar order of magnitude as the measured errors. For this reason the measurements are filtered to the time range of $8 - 210 \mu\text{s}$ as shown in Figure 3(c) and (d). Figure 3(d) shows the pattern, that most curves first decline, but all curves increase in later times.

The apparent resistivities of the anomalous soundings as seen in Figure 4(b) show no clear pattern due to high distortions in the curves. These soundings (M014, M043, M044) are located close to a road as Figure 1 shows, which could explain the poor data quality. These anomalous measurements were still processed, to test how well they compare to the other soundings. In order to make it more comparable the same time range of $8 - 210 \mu\text{s}$ was used for the filtering (Figure 4(d)).

The normal soundings (Figure 5) and anomalies (Figure 6) of the second survey (8th October 2024) with the 6.25×6.25 m loop were processed in a similar fashion. Compared to Figure 3(b) Figure 5(b) shows the effects of the turn-off ramp until $12 \mu\text{s}$, but only for the soundings within the lake (M057-M065, except for M062), while the other soundings show effects until $7 \mu\text{s}$, which should be a bit smaller for smaller loop sizes (Aigner et al. 2021). The long lasting effect of the turn-off ramp for the soundings in the water, can on one side be attributed to a longer turn-off ramp in water (Aigner et al. 2021) and can on the other hand also be due to the loop being partially submerged during the measurements, which breaks the assumption of

a layered halfspace, which is necessary for the computation for the apparent resistivity as well as the data inversion (Kirsch 2006). Due to the smaller loop size, the curves become distorted much earlier at about $85 \mu\text{s}$ (Figure 5(b)) and at that time the impulse response also becomes the same order of magnitude as the measured error (Figure 5(a)). In order to make processing easier the soundings in and next to the lake were both filtered to the time range $12 - 80 \mu\text{s}$ as shown in Figure 5(c) and (d). Figure 5(d) shows that in contrast to the soundings with the larger loop, the curves only show the incline at the end, but not the decline in the beginning.

For the second survey the anomalous soundings, shown in Figure 6, include the soundings M009 and M010, which show distortions, but also M002, which has much lower apparent resistivities (about $10 - 15 \Omega\text{m}$ less) compared to the other soundings, and M024, which has much higher apparent resistivities (about $15 - 30 \Omega\text{m}$ higher) compared to the other soundings. For the anomalous soundings the same time range of $12 - 80 \mu\text{s}$ was used for the filtering (Figure 5(c) and (d)). Figure 6(d) shows that due to the distortions no clear pattern can be seen in the soundings M009 and M010, M024 shows a much steeper incline than the other soundings (Figure 5(d)), and M002 shows a decline in the apparent resistivity curve. Figure 2 shows that M009 and M010 are close to a road and M002 is close to a vineyard containing metall bars.

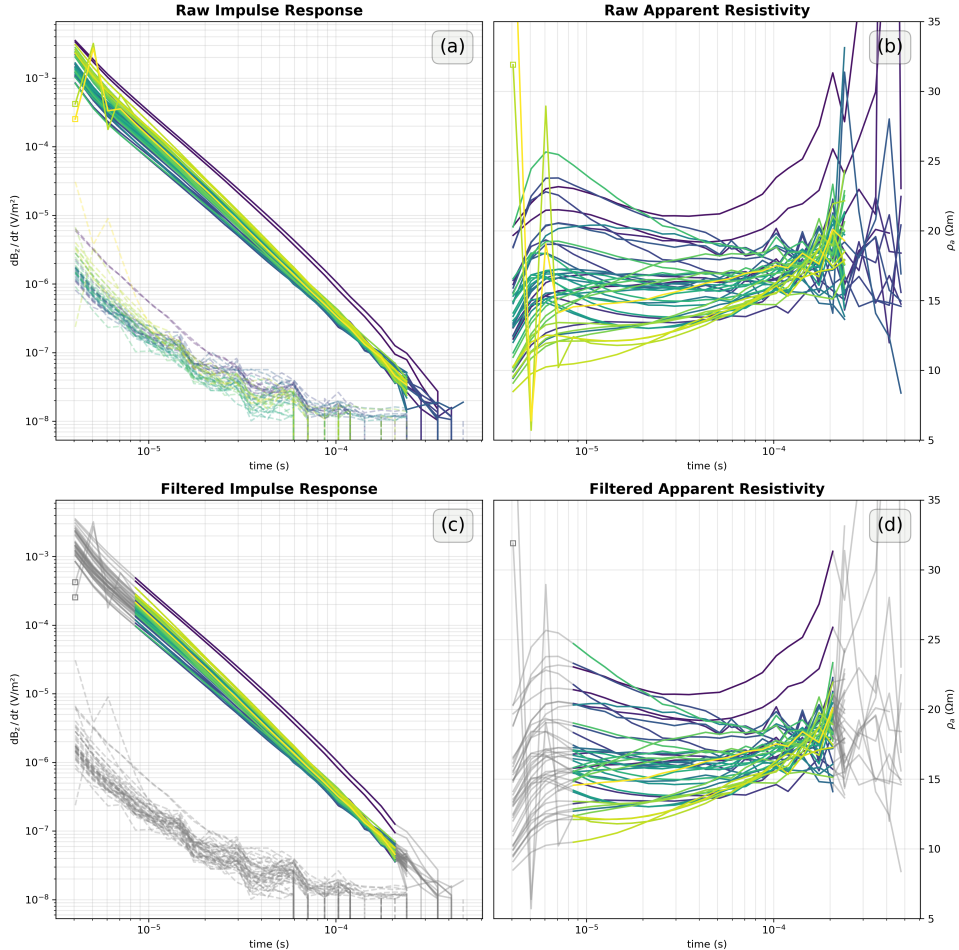


Fig. 3: Raw and filtered impulse responses and apparent resistivities from the 22nd May 2024 survey, where anomalies are excluded. The first sounding (M001) is colored dark purple, the last sounding (M045) is yellow, and all soundings in between are assigned a color from a uniform distribution between the two border colors. Subfigure (a) shows the raw impuls response as well as the measured errors as dashed lines, (b) shows the computed apparent resistivities, (c) show the filtered impulse response, the measured error as dashed lines, and greyed out raw data as comparison, (d) shows the resulting filtered apparent resistivities and greyed out raw values.

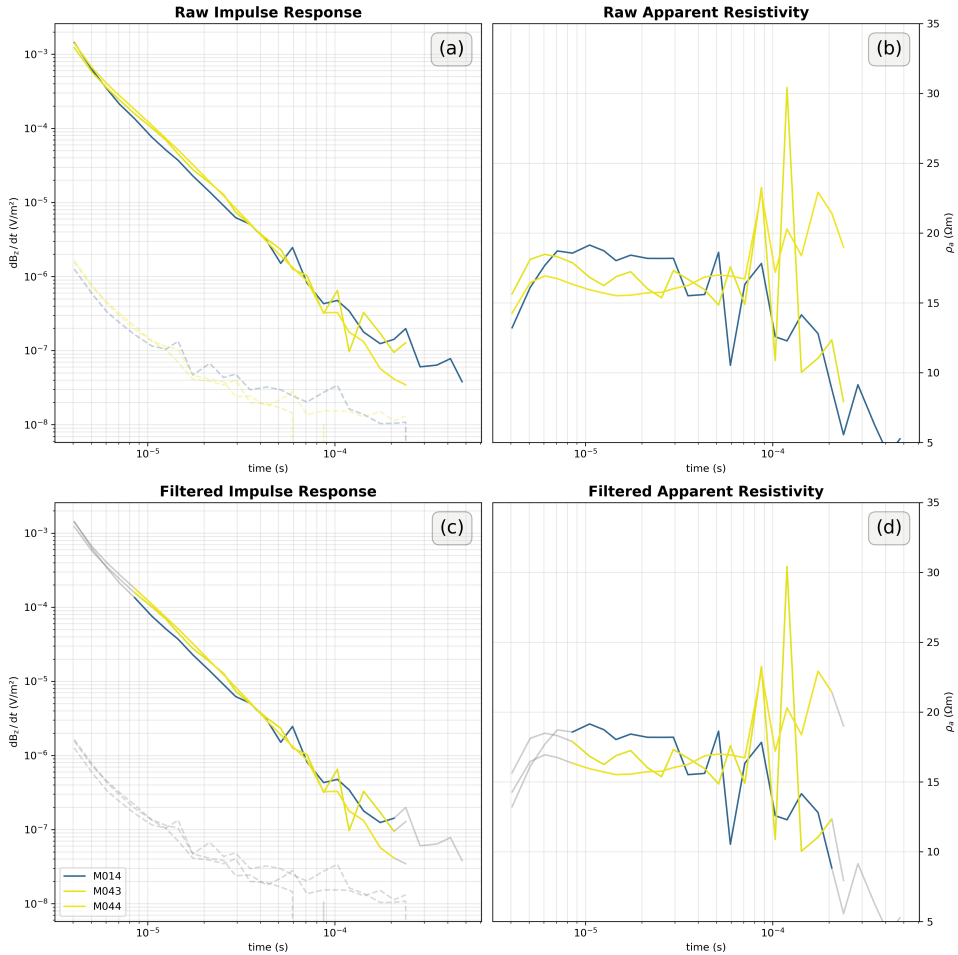


Fig. 4: The anomalous raw and filtered impulse responses and apparent resistivities from the 22nd May 2024 survey. Subfigure (a) shows the raw impuls response as well as the measured errors as dashed lines, (b) shows the computed apparent resistivities, (c) show the filtered impulse response, the measured error as dashed lines, and greyed out raw data as comparison, (d) shows the resulting filtered apparent resistivities and greyed out raw values.

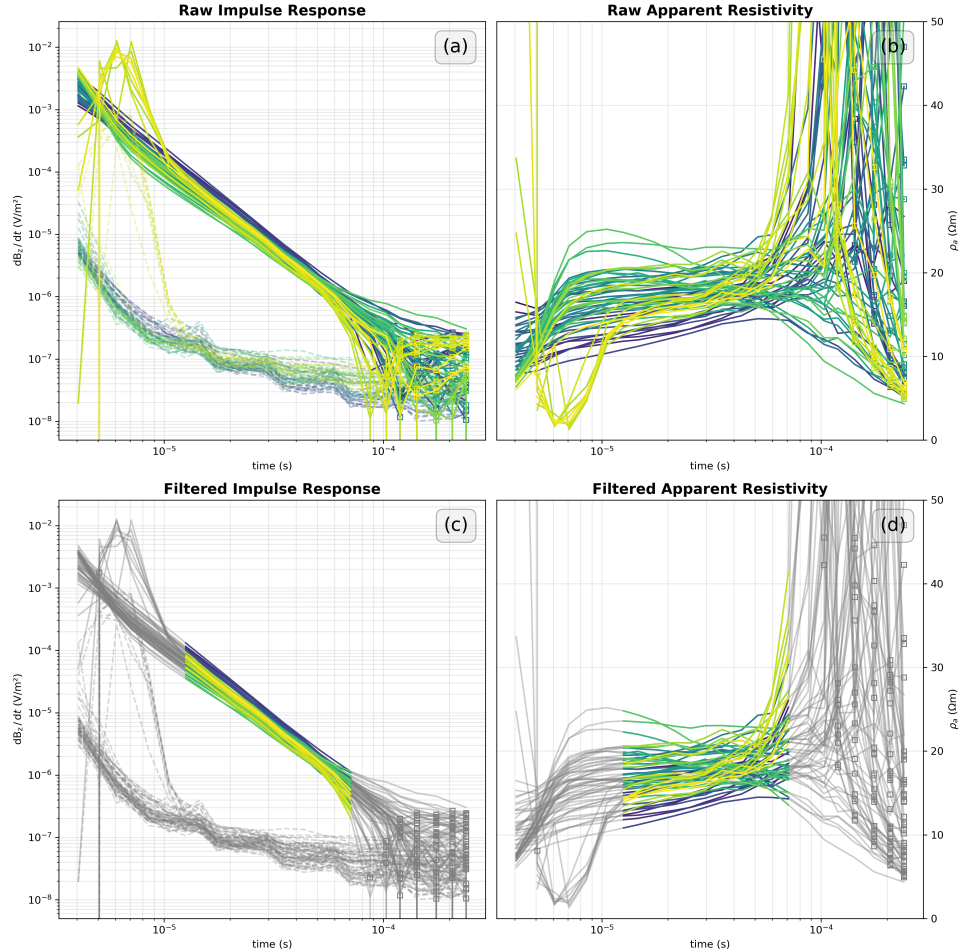


Fig. 5: Raw and filtered impulse responses and apparent resistivities from the 8th October 2024 survey, where anomalies are excluded. The first sounding (M001) is colored dark purple, the last sounding (M066) is yellow, and all soundings in between are assigned a color from a uniform distribution between the two border colors. Subfigure (a) shows the raw impulse response as well as the measured errors as dashed lines, (b) shows the computed apparent resistivities, (c) shows the filtered impulse response, the measured error as dashed lines, and greyed out raw data as comparison, (d) shows the resulting filtered apparent resistivities and greyed out raw values.

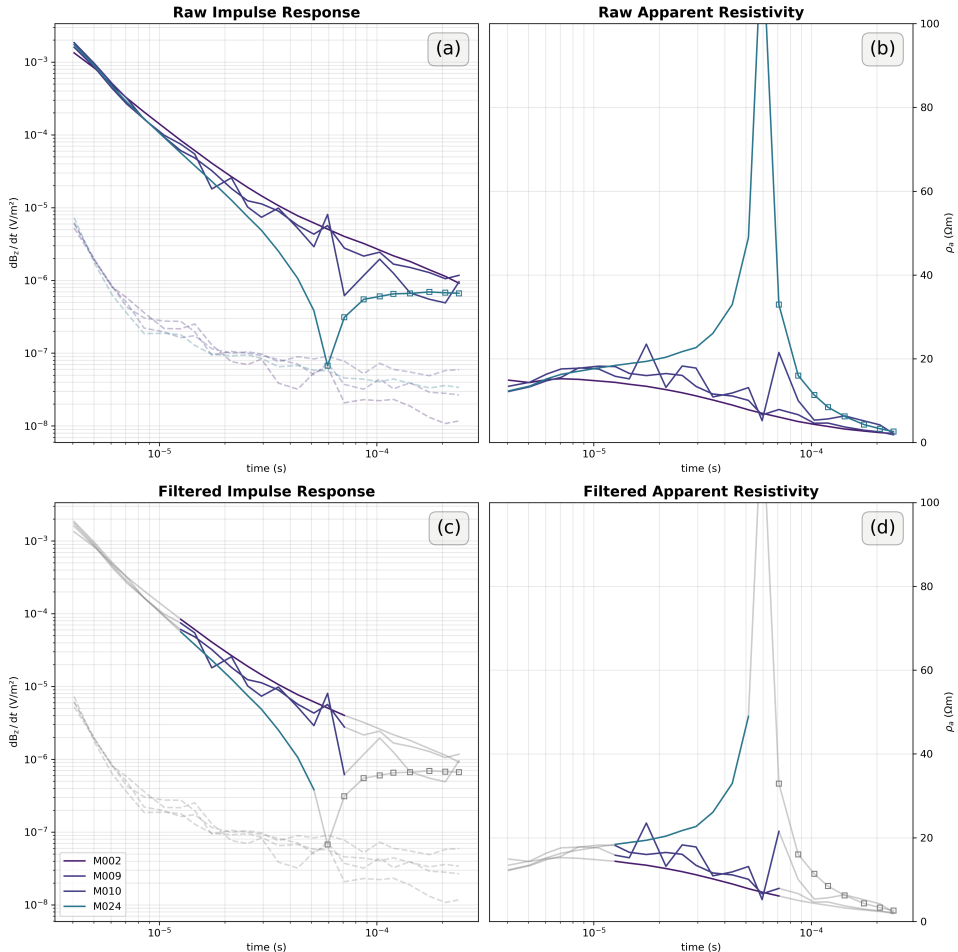


Fig. 6: The anomalous raw and filtered impulse responses and apparent resistivities from the 8th October 2024 survey. Subfigure (a) shows the raw impuls response as well as the measured errors as dashed lines, (b) shows the computed apparent resistivities, (c) show the filtered impulse response, the measured error as dashed lines, and greyed out raw data as comparison, (d) shows the resulting filtered apparent resistivities and greyed out raw values.

3.2 Inversion Parameters

The inversion algorithm (Aigner et al. 2021) used for the inversion needs various starting parameters. One of which is the layer distribution, which specifies the number and thicknesses of the layers characterising the subsurface model, which is used for the inversion. Welkens (2025) shows that model with 1 m-Layers until 5 m depth and 1.5 m-Layers below that, until a maximal depth of 10 m optimises the inversion speed and model fit for data gathered with a 6.25×6.25 m loop and 4.1 A of current. Since a 12.5×12.5 m loop is used in the first survey and

Figure 7(c) shows that the inversion algorithm struggles to fit the late time data. Figure 8(c) shows that this issue can be resolved by choosing a maximal depth of 10 m.

Regarding the noise floor, the minimum value for the relative error used in the inversion, Aigner et al. (2024) used 1.5 – 2.5 % for the measurements with a 12.5×12.5 m and a 50.0×50.0 m loop the in the soda lakes and 3 – 15 % for the soundings at the ice glacier. For the first survey with the 12.5×12.5 m loop a noise floor of 2.5 % was chosen because this measurement configuration resembles the configuration with the smaller loop by Aigner et al. (2024). For the second survey with the 6.25×6.25 m loop the noise floor was set to 8.0 % because smaller loop sizes decreases the magnetic moment, which leads to a smaller signal-to-noise ratio and thus to less reliable measurements (Kirsch 2006).

To compute the L-Curve and find an optimal lambda value for the inversion, a range of logarithmically spaced lambda values was chosen with the lower boundary of 10, the upper boundary of 1000, and a total of 20 values. This range covers the lambda values Aigner et al. (2024) used for the inversion of the data gathered in the soda lakes (50) and the former graphite mine (500 to 1000). By choosing 20 values in total total computation time is kept low, while the characteristics of each L-Curve can still be resolved (Figure 9).

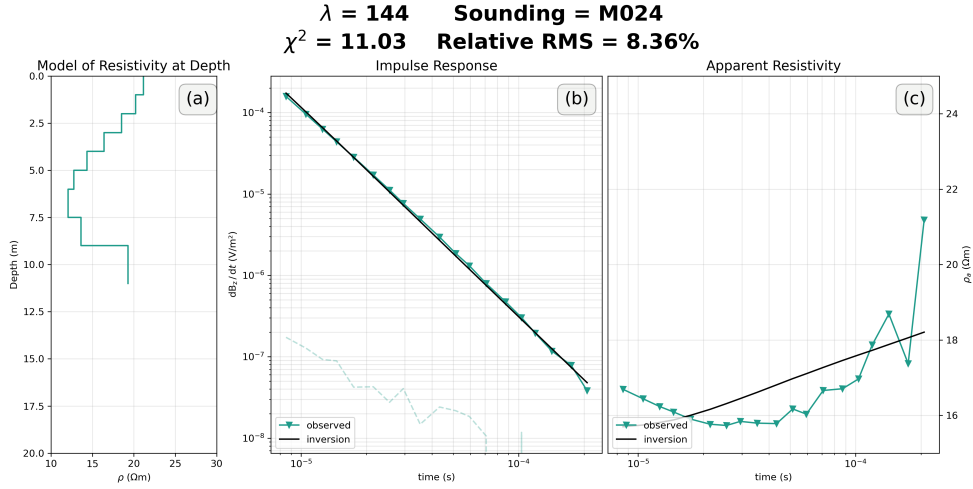


Fig. 7: Inversion results for a representative sounding (M024) for the first survey (22nd May 2024) with the layer distribution of 1 m thicknesses until 5 m depth and 1.5 m until 10 m depth. Subfigure (a) shows the final subsurface model of the resistivity, (b) shows the comparison between the modelled and measured impulse response as well as the measured error as a dashed line, (c) shows the comparison between the modelled and measured apparent resistivities.

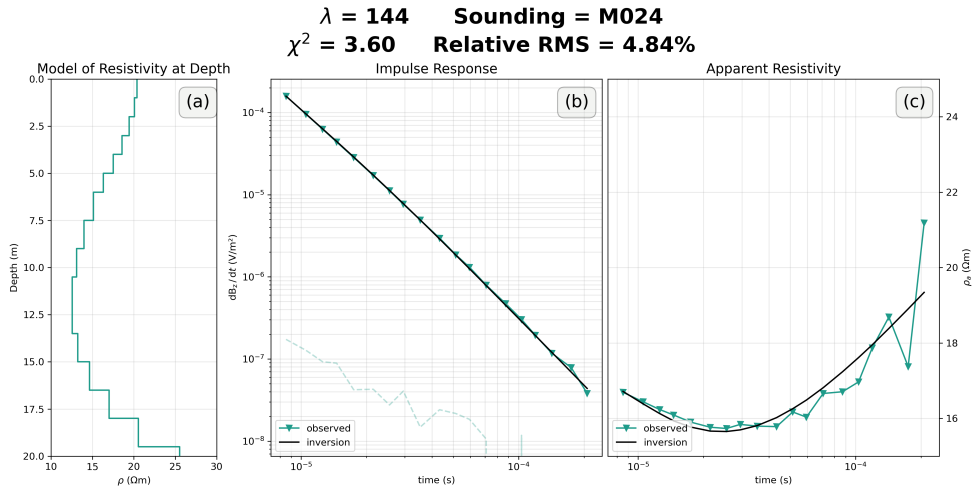


Fig. 8: Inversion results for a representative sounding (M024) for the first survey (22nd May 2024) with the layer distribution of 1 m thicknesses until 5 m depth and 1.5 m until 20 m depth. Subfigure (a) shows the final subsurface model of the resistivity, (b) shows the comparison between the modelled and measured impulse response as well as the measured error as a dashed line, (c) shows the comparison between the modelled and measured apparent resistivities.

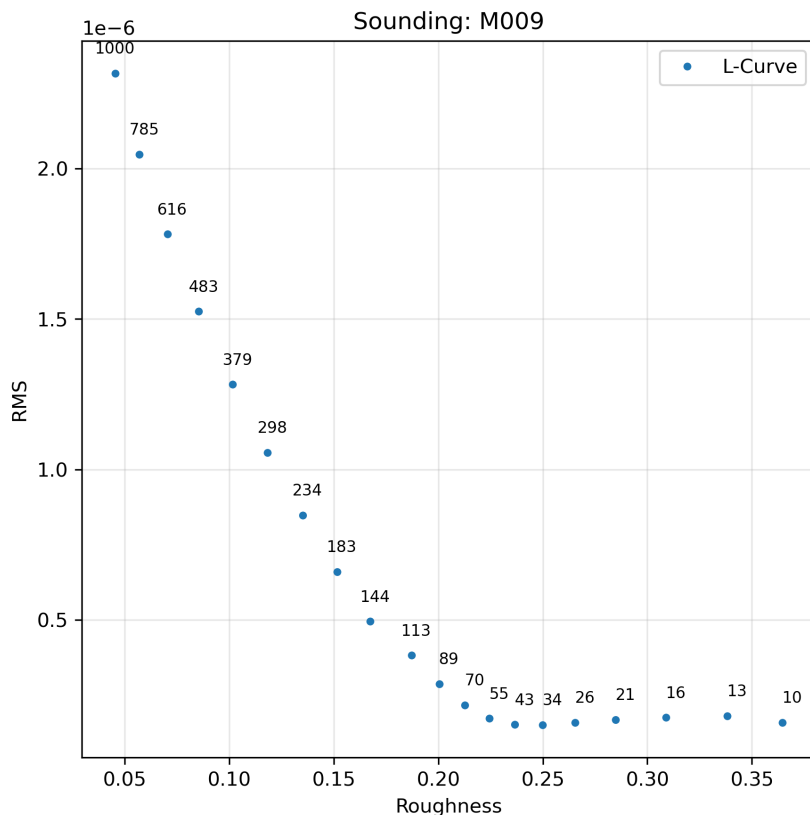


Fig. 9: L-Curve of the sounding M009 of the first survey (22nd May 2024) showcasing the chosen distribution of lambda values. The number next to each point is the corresponding lambda value. The y-axis shows the root-mean-square (RMS) misfit between the model and the measured data. The x-axis shows the roughness of the model.

3.3 Finding an Optimal Lambda

Figure 9 shows that the RMS misfit ($0.1 - 2.5e-6$) and the roughness ($0.04 - 0.37$) are of entirely different orders of magnitude. To highlight this issue the various search algorithms were applied to the sounding M010 of the first survey, shown in Figure 11, where due to its minor curvature all three algorithms return a too high lambda value between $483 - 616$ as opposed to the visual optimum at about 33.6. To counteract this a linear normalisation, using the formula $a_i = \frac{a_i - a_{\min}}{a_{\max} - a_{\min}}$, was applied to both RMS and roughness. Figure 11 shows how with the normalisation all three search algorithms return a value ($25 - 43$) around the visual optimum of 33.6. Hence all further searches for an optimal lambda were carried out with the normalisation.

Figure 9 shows how the ideal L-Curve would look like as it was described by Hansen (1999) and Farquharson et al. (2004), but TEM data gathered in the field always includes some level of noise, which can lead differently shaped resulting curves from this computation. One extreme example can be seen in Figure 12, which resembles a random cluster of points rather than an L-Curve, which makes discerning an optimal lambda not feasible. Both the cubic spline as well as the gradient based algorithm find a local

minimum (Figure 12), but as the plotted data points do not create a cohesive L-Curve, hence the returned values not be considered the actual optimal lambda for the inversion.

Another example where the L-curve differs from the ideal can be seen in Figure 13, which shows an minimum at the lambda value 379 and an increase in the RMS misfit afterwards until the lambda value 55. This could possibly be explained by the inversion algorithm trying to fit the model to an error in the measured data, which would explain the increase in the RMS misfit. Figure 13 shows that both the cubic spline and gradient based algorithm can find this minimum. Only the golden section search fails, which can be explained by the minimum being close to the upper boundry and thus being discarded in the first iteration of the search algorithm. Cultrera et al. (2020) described that the first two lambda values within the interval are calculated using the golden section method, which in this case excludes the lambda value associated with the minimum.

Another eventuality can be seen in Figure 14, where the curve shows a discontinuity between the lambda values 43 and 34, where the RMS misfit abruptly decreases by about 70 %. Figure 14 shows that the golden section search and the gradient based algorithm can still find this optimal lambda value, but the cubic spline algorithm can not and returns a value before the discontinuity.

An additional case is shown by Figure 15, where the roughness values start to decrease again after the lambda value of about 20 and thus "looping back". This could be caused by the inversion algorithm trying to fit the erroneous data points and thus prioritising outliers over following the general trend. If for example an outlier opposes a general trend, which indicates a multiple layers with differing resistivities, then by fitting the outlier leads to a more homogeneous model and thus a decrease in the model roughness. Figure 15 shows that the golden section search returns the lambda value at the turning point as opposed to the actual optimum, which both the cubic spline and gradient based algorithms return.

These examples highlight the strengths and shortcomings of each search algorithm. Table 3 shows a summary of how the algorithms

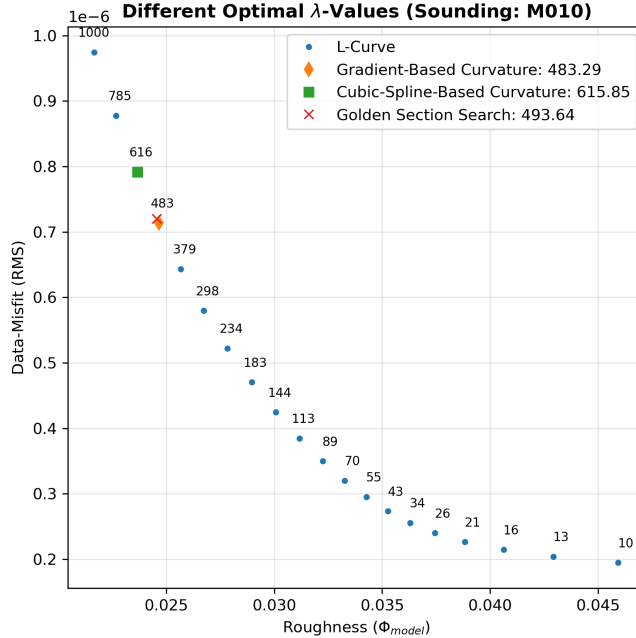


Fig. 10: Automatically searching for an optimal lambda of the sounding M010 in the first survey (22nd May 2024) without applying a normalisation to the L-Curve.

performed overall and comparing this to a visual inspection of the generated L-Curve. In both surveys 7 out of 111 soundings produce a curve, which can not be used to find an optimal lambda, even when visually inspected. The golden section search found the least optimal lambdas, only 57 out of 111, but when it worked, it returned the most accurate results by finding the optimal lambda accurately down to first decimal point. The cubic spline algorithm was more reliable overall by finding 83 out of 111 optimal lambdas, but as Figure 14 shows it also struggles with suboptimal L-Curves. In our analysis the gradient based curvature analysis yielded the most promising results by finding 89 out of 111 optimal lambda values, hence it was used to find the optimal lambda for each sounding respectively. As all search algorithms maximise the curvature of the L-Curve to find the lambda, all of them struggle with curves with minimal curvature or even linear graphs. Table 3 also shows that there are minimal differences in the produced L-Curves as well as the effectiveness of the automated search algorithms between the two surveys and thus the two measuring configurations. All comparison plots can be found at https://github.com/pb-tuwien/BSc_Soda_Lakes_Balogh.git

under "data/2024xxxx/TEMdata/07-inversion_analysis/comparison_M0yy.png", where xxxx is either "0522" for the first or "1008" for the second survey and yy being the sounding number (either 01 to 45 or 01 to 66).

Tab. 3: Summary of the search for an optimal lambda for each sounding, comparing the visual identification with the various automated search algorithms.

Search Type	Found	Not Found
22nd May 2024		
Visual	42	3
Cubic Spline	32	13
Gradient Based	34	11
Golden Section	19	26
8th October 2024		
Visual	62	4
Cubic Spline	51	15
Gradient Based	55	11
Golden Section	38	28

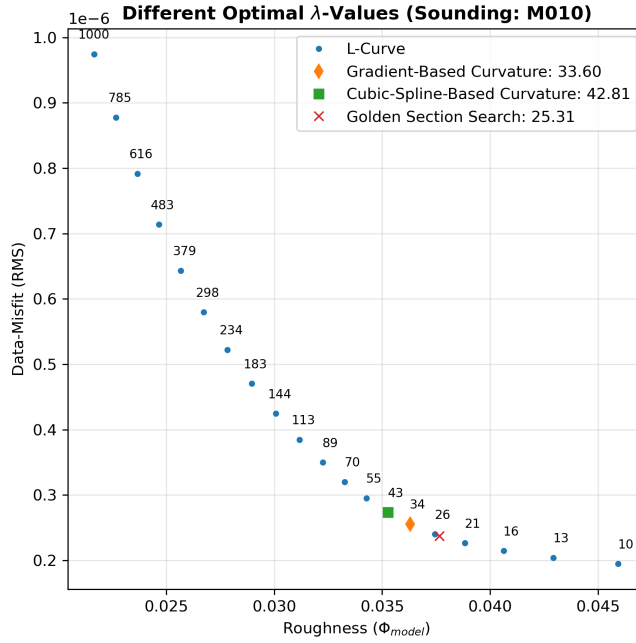


Fig. 11: Automatically searching for an optimal lambda of the sounding M010 in the first survey (22nd May 2024) while applying a normalisation to the L-Curve.

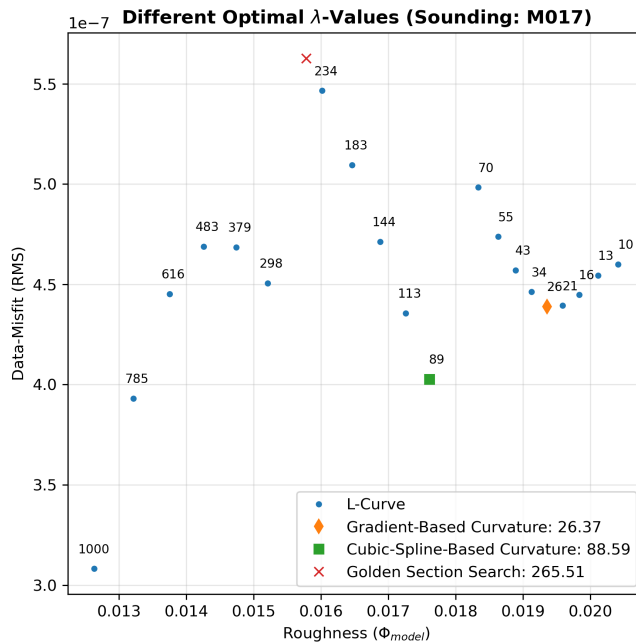


Fig. 12: Automatically searching for an optimal lambda of the sounding M017 in the first survey (22nd May 2024), which showcases how the search algorithms perform, when no expected characteristic of an L-curve can be found.

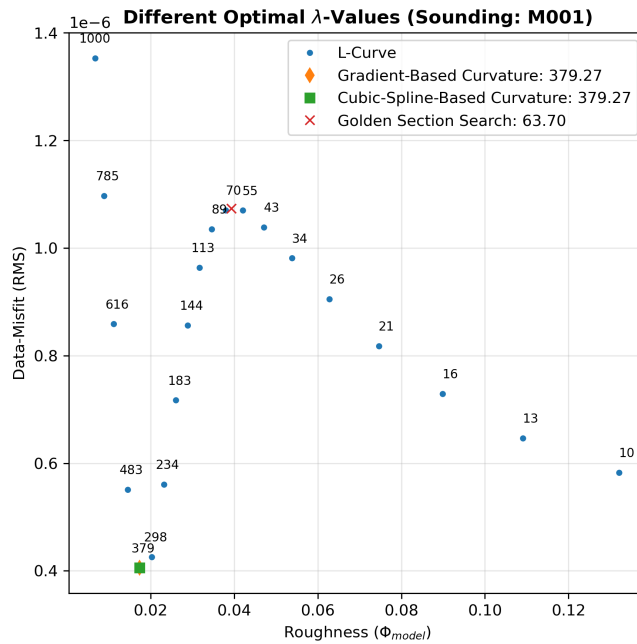


Fig. 13: Automatically searching for an optimal lambda of the sounding M001 in the second survey (8th October 2024), which showcases that the golden section search algorithm is unable to identify a minimum close to a boundary.

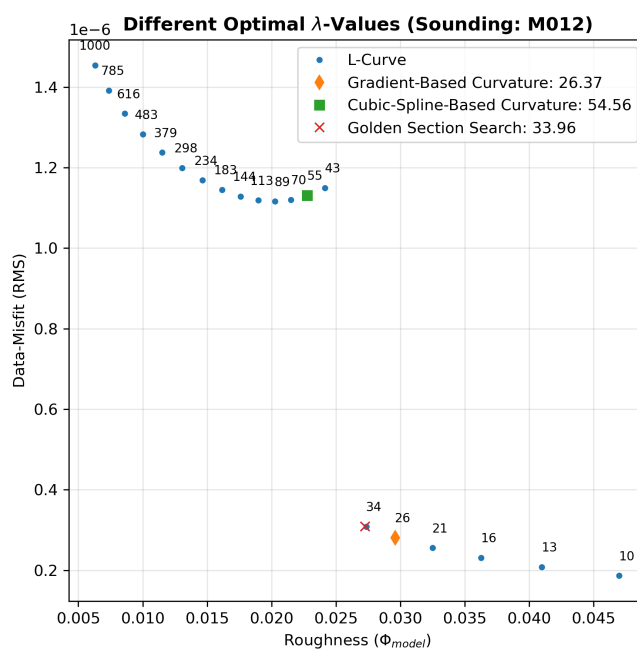


Fig. 14: Automatically searching for an optimal lambda of the sounding M012 in the second survey (8th October 2024), which showcases that the search algorithm fitting a cubic spline function can not optimise the lambda for an L-Curve with a discontinuity.

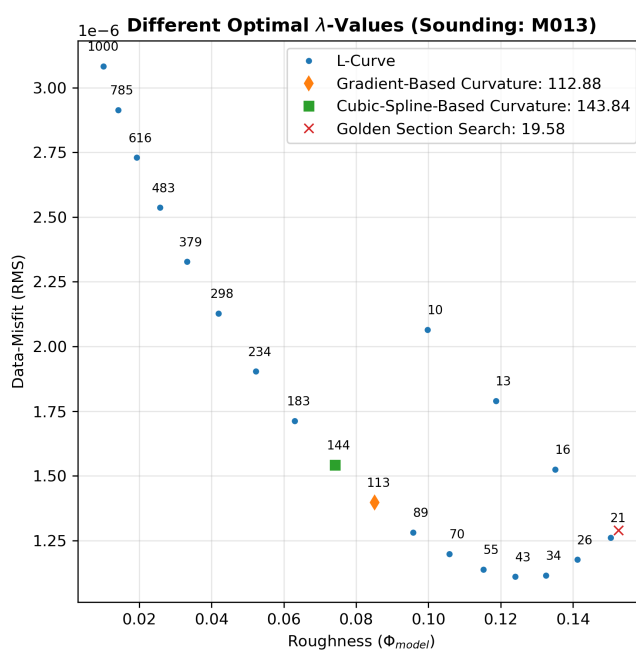


Fig. 15: Automatically searching for an optimal lambda of the sounding M013 in the first survey (22nd May 2024), which showcases how the golden section search algorithm fails, when L-curve shows an inverted C-shape on the end.

3.4 Comparing Inversion Results

With these findings, we finally obtained the necessary parameters for running the inversions, which enables a comparison of different resistivity models obtained from the various measuring configurations, as described in Table 2. Because the late time data was filtered due to a high noise level, the different time keys are not considered and only the different injected currents and the loop sizes are compared. Ideally the compared soundings, would be at the same location, which is why we chose the soundings M028 (shown in Figure 16) of the first and M052 (shown in Figure 17) of the second survey, which use the 12.5×12.5 m loop with 1.0 A of current and 6.25×6.25 m loop with 4.1 A of current. Figures 1 and 2 show that these two broadly align. For the configuration 12.5×12.5 m loop with 4.1 A of current we do not have a sounding at the same location, but sounding M002 (shown in Figure 18) of the first survey is also in the north of the Martenhofer Lacke (Figure 1). Figure 16(c) shows how with the large loop three distinct layers can be found: A 5 m-layer with $17.5 \Omega\text{m}$, a second 11 m-layer with $13.5 \Omega\text{m}$, and the start of a third layer with $22 \Omega\text{m}$. The model seems to fit the data adequately as can

be seen in Figure 16(a) and (b), which is also supported by a relative RMS misfit of 4.77 %.

For the same location five months later the small loop with 4.1 A produces a model with only two discernable layers, as seen in Figure 17(c): A 5 m-layer with $16 \Omega\text{m}$ and the start of a second layer with $24 \Omega\text{m}$. The second layer is not distinctly visible, but rather a gradual increase, which corresponds with the almost linearly increasing apparent resistivity curve in Figure 17(b). Figure 17(a) and (b) also show that the last measured data point possibly indicates a change in the slope and thus a new layer (Fitterman et al. 1986), but it could also be data noise.

Figure 18 represents the measurements made with the large loop as well as 4.1 A and in (c) similar three layers can be seen as in Figure 16(c) but with differing resistivity values: A 5 m-layer with $31 \Omega\text{m}$, a second 12 m-layer with $13.5 \Omega\text{m}$, and the start of a third layer with $30 \Omega\text{m}$. Figure 18(b) shows that the model does not quite fit the measured data, but follows the general trend of the curve.

We found that the measurements with the 12.5×12.5 m loop were able to discern the same three layers regarding the thicknesses, which Aigner et al. (2024) found in a borehole at the soda lakes, which is located about 1.5 km north-east of the Martenhofer Lacke. Aigner et al. (2024) describes a 1.6 m clay-silt layer, followed by a 5.4 m sandy gravel aquifer, and a second clay-silt layer until the maximal drilled depth of 10 m. Figures 16 and 18 both show in subfigure (c) that the first two layers of the borehole can not be differentiated and are shown as one layer with the resistivities of $31 \Omega\text{m}$ and $17.5 \Omega\text{m}$ respectively. These differences could be caused by differing clay-silt layer and aquifer thicknesses, which also changes the influence of each over the resistivity value representing the combined resistivities of both layers. The second layer present in the subfigures (c) of Figures 16 and 18 shows a layer with a resistivity of about $13.5 \Omega\text{m}$, which points to a clay-silt layer when compared with the values in ??

(Referencing table with common resistivity

from the State of the Art). This agrees well with the borehole data described by Aigner et al. (2024). The third layer with the resistivity

of $22\Omega\text{m}$ and $30\Omega\text{m}$ respectively, could indicate a second aquifer, which was also detected by Aigner et al. (2024), who found that a second aquifer with the resistivity value of $30\Omega\text{m}$ at a depth below 35 m.

The model created through the data gathered with the $6.25 \times 6.25\text{ m}$ loop, as seen in Figure 17, only shows the first two layers and is unable to resolve the third layer. The advantage of being able to resolve shallow layers with a smaller loop (Kirsch 2006), is counteracted by the effects of turn-off ramp as described by Aigner et al. (2021) and thus the need to discard the early time data. The results produced with the larger loop and the current of 4.1 A seem to reproduce the results of earlier studies like Aigner et al. (2024) the best out of the configurations tested in this work.

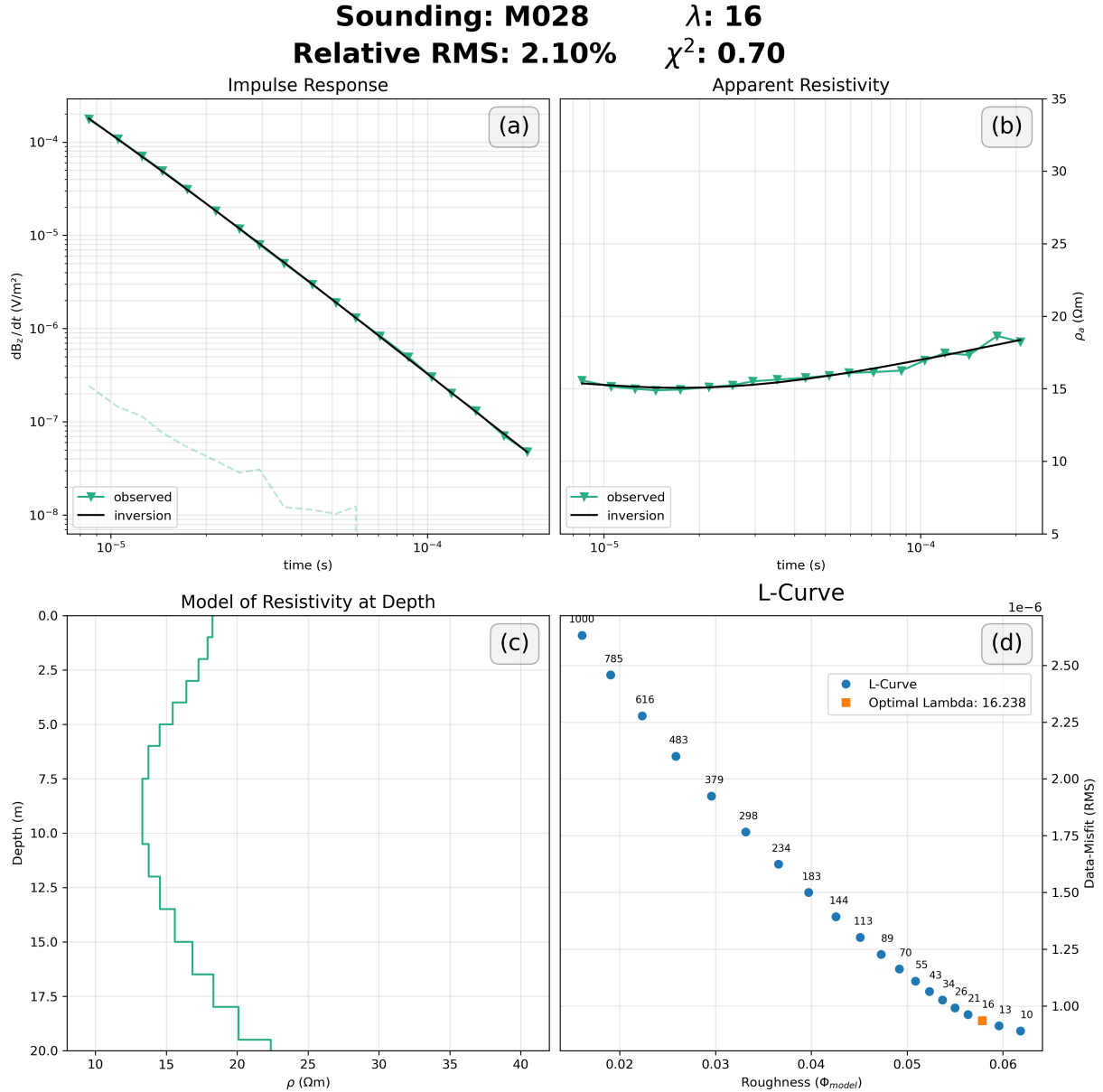


Fig. 16: Optimised inversion of the sounding M028 of the first survey, which was measured with a $12.5 \times 12.5 \text{ m}$ loop and 1.0 A of current. This sounding was done at the same location as M052 of the second survey. Subfigure (a) shows the comparison between modelled and measured impulse response as well as the measured error, (b) shows the comparison between modelled and measured apparent resistivities, (c) shows the final subsurface model of the resistivity, (d) shows the L-curve of this sounding with the chosen lambda value marked in orange.

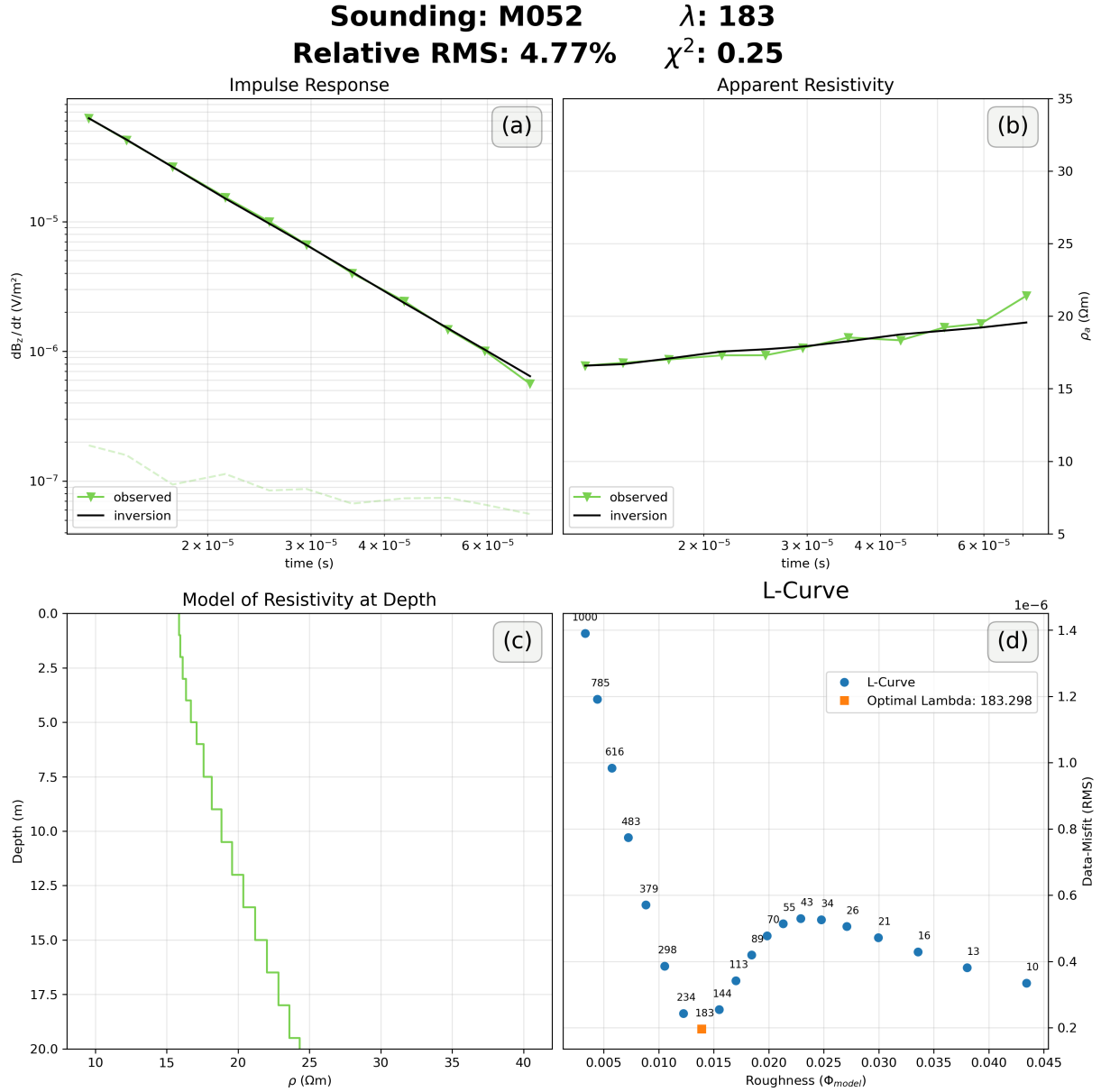


Fig. 17: Optimised inversion of the sounding M052 of the second survey, which was measured with a 6.25×6.25 m loop and 4.1 A of current. This sounding was done at the same location as M028 of the first survey. Subfigure (a) shows the comparison between modelled and measured impulse response as well as the measured error, (b) shows the comparison between modelled and measured apparent resistivities, (c) shows the final subsurface model of the resistivity, (d) shows the L-curve of this sounding with the chosen lambda value marked in orange.

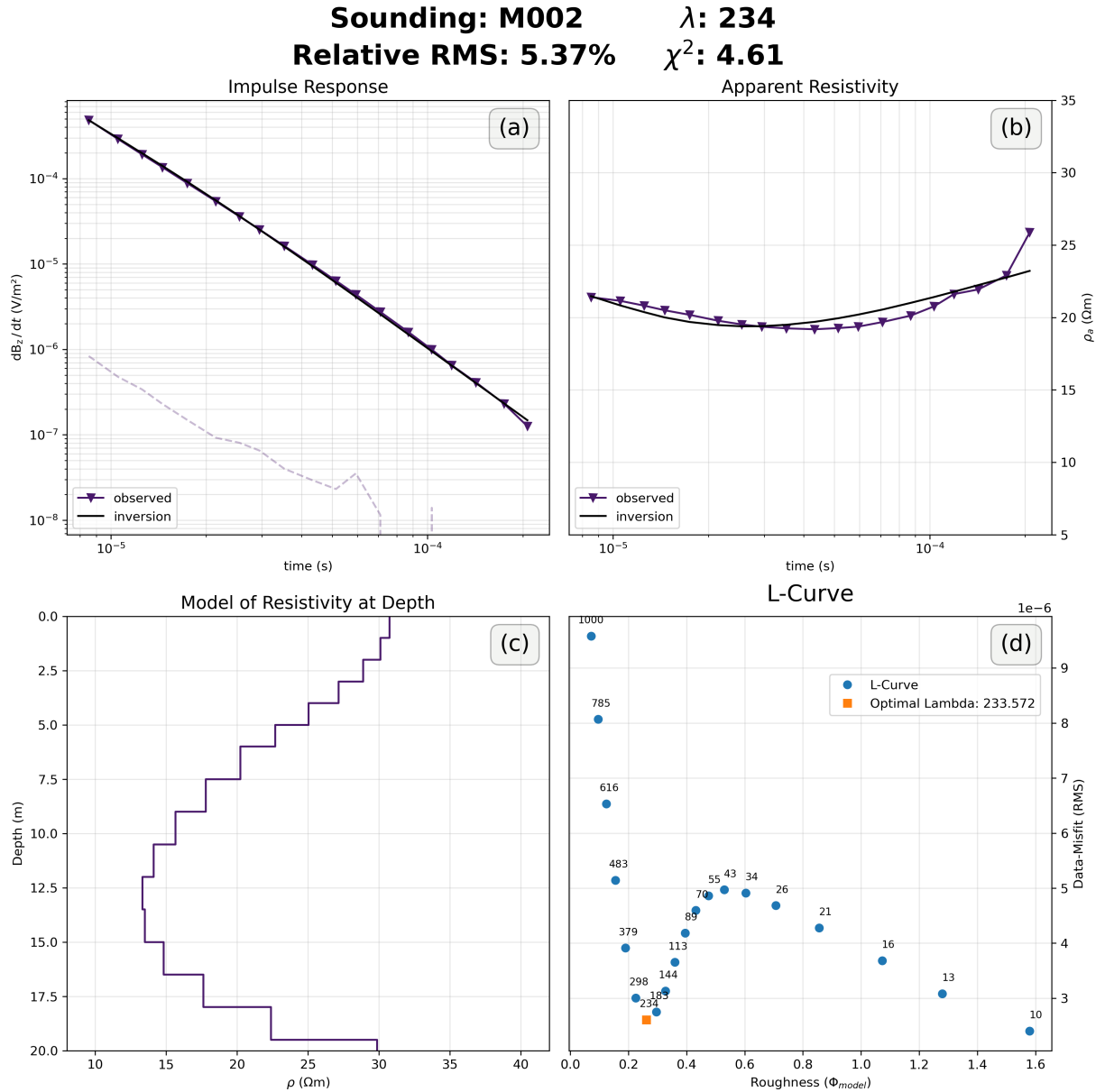


Fig. 18: Optimised inversion of the sounding M002 of the first survey, which was measured with a 12.5×12.5 m loop and 4.1 A of current. Subfigure (a) shows the comparison between modelled and measured impulse response as well as the measured error, (b) shows the comparison between modelled and measured apparent resistivities, (c) shows the final subsurface model of the resistivity, (d) shows the L-curve of this sounding with the chosen lambda value marked in orange.

4 Conclusion

List of Figures

1	Map of Sounding Locations in May	2
2	Map of Sounding Locations in October	3
3	Response Curves of the May Survey	5
4	Anomalous Responses of the May Survey	6
5	Response Curves of the October Survey	7
6	Anomalous Responses of the October Survey	8
7	Inversion With 10m Maximum Depth	10
8	Inversion With 20m Maximum Depth	10
9	Example L-Curve	11
10	Lambda Search Without Normalisation	13
11	Lambda Search With Normalisation	14
12	Example Lambda Search: Bad Curve	14
13	Example Lambda Search: Minimum Close to Boundary	15
14	Example Lambda Search: Curve With a Discontinuity	15
15	Example Lambda Search: Curve With a "Loop-Back"	16
16	Inversion of Sounding with the Large Loop and Small Current .	19
17	Inversion of Sounding with the Small Loop and Large Current .	20
18	Inversion of Sounding with the Large Loop and Large Current .	21

List of Tables

1	Time Key Parameters of the TEM-FAST Device	2
2	Device Settings in Both Surveys	3
3	Summary of the search for an optimal Lambda	13

Declaration of competing interest

The authors declare that they have no known competing financial interests or personal rela-

tionships that could have appeared to influence the work reported in this thesis.

Data availability

The python package for this thesis was developed in cooperation with Jakob Welkens and is building upon the routine from Aigner et al. (2021). It is available open-source and can be accessed on github (https://github.com/pb-tuwien/Bsc_TEM_tools.git). To facilitate full reproducibility of the results all data and python routines used throughout this work can also be accessed on github (https://github.com/pb-tuwien/BSc_Soda_Lakes_Balogh.git)

References

- Aigner, L., P. Högenauer, M. Bücker, and A. Flores Orozco (2021). "A flexible single loop setup for water-borne transient electromagnetic sounding applications". In: *Sensors* 21.19, p. 6624.
- Aigner, L., D. Werthmüller, and A. F. Orozco (2024). "Sensitivity analysis of inverted model parameters from transient electromagnetic measurements affected by induced polarization effects". In: *Journal of Applied Geophysics* 223, p. 105334.
- Barsukov, P. O., E. B. Fainberg, and E. O. Khabensky (2015). "Shallow investigations by TEM-FAST technique: methodology and examples". In: *Electromagnetic sounding of the Earth's interior*. Elsevier, pp. 47–78.
- Boros, E. and L. Vörös (2025). "How can unique alkaline soda waters be managed and restored? Lake Neusiedl as the largest threatened european example". In: *Ecohydrology* 18.2, e2738.
- Cultrera, A. and L. Callegaro (2020). "A simple algorithm to find the L-curve corner in the regularisation of ill-posed inverse problems". In: *IOP SciNotes* 1.2, p. 025004.
- Farquharson, C. G. and D. W. Oldenburg (2004). "A comparison of automatic techniques for estimating the regularization parameter in non-linear inverse problems". In: *Geophysical Journal International* 156.3, pp. 411–425.

- Fitterman, D. V. and M. T. Stewart (1986). “Transient electromagnetic sounding for groundwater”. In: *Geophysics* 51.4, pp. 995–1005.
- Hansen, P. C. (1999). “The L-curve and its use in the numerical treatment of inverse problems”. In.
- Kirsch, R. (2006). *Groundwater geophysics: a tool for hydrogeology*. Springer.
- Lloyd, J., C. Taylor, R. Lawson, and R. Shields (1997). “The use of the L-curve method in the inversion of diffusion battery data”. In: *Journal of aerosol science* 28.7, pp. 1251–1264.
- Rücker, C., T. Günther, and F. M. Wagner (2017). “pyGIMLi: An open-source library for modelling and inversion in geophysics”. In: *Computers & Geosciences* 109, pp. 106–123.
- Welkens, J. (2025). “Comparison of subsurface geophysical models of Hutweidenlacke (Nationalpark Seewinkel) based on the Transient Electromagnetic Method”. MA thesis. Research Unit Geophysics, Department of Geodesy and Geoinformation, TU Wien, Vienna, Austria.
- Werthmüller, D. (2017). “An open-source full 3D electromagnetic modeler for 1D VTI media in Python: empymod”. In: *Geophysics* 82.6, WB9–WB19. DOI: 10.1190/geo2016-0626.1. URL: <https://doi.org/10.1190/geo2016-0626.1>.